Delft University of Technology

Observation and Modeling of Near-Bistable Dark-Mode Current-Voltage Characteristics in Semi-Insulating Gallium Arsenide with Implications for Photoconductors

Dong, Yicong; Dowling, Karen; Ghandiparsi, Soroush; Voss, Lars; Rakheja, Shaloo

DOI
10.1109/JEDS.2023.3291312

Publication date
2023

Document Version
Final published version

Published in
IEEE Journal of the Electron Devices Society

Citation (APA)
Dong, Y., Dowling, K., Ghandiparsi, S., Voss, L., & Rakheja, S. (2023). Observation and Modeling of Near-Bistable Dark-Mode Current-Voltage Characteristics in Semi-Insulating Gallium Arsenide with Implications for Photoconductors. *IEEE Journal of the Electron Devices Society*, *11*, 385-398. https://doi.org/10.1109/JEDS.2023.3291312

Important note
To cite this publication, please use the final published version (if applicable).
Please check the document version above.

Copyright
Other than for strictly personal use, it is not permitted to download, forward or distribute the text or part of it, without the consent of the author(s) and/or copyright holder(s), unless the work is under an open content license such as Creative Commons.

Takedown policy
Please contact us and provide details if you believe this document breaches copyrights.
We will remove access to the work immediately and investigate your claim.

This work is downloaded from Delft University of Technology.
For technical reasons the number of authors shown on this cover page is limited to a maximum of 10.

Received 19 December 2022; revised 2 April 2023 and 22 May 2023; accepted 25 June 2023. Date of publication 30 June 2023; date of current version 20 July 2023. The review of this article was arranged by Editor S. Krishnamoorthy.

Digital Object Identifier 10.1109/JEDS.2023.3291312

Observation and Modeling of Near-Bistable Dark-Mode Current-Voltage Characteristics in Semi-Insulating Gallium Arsenide With Implications for Photoconductors

YICONG DONG [1], KAREN DOWLING [2,3] (Member, IEEE), SOROUSH GHANDIPARSI [2] (Member, IEEE), LARS VOSS [2], SHALOO RAKHEJA [1] (Senior Member, IEEE)

1 Holonyak Micro and Nanotechnology Laboratory, University of Illinois at Urbana–Champaign, Urbana, IL 61801, USA
2 Materials Engineering Division, Lawrence Livermore National Laboratory, Livermore, CA 94550, USA
3 Department of Microelectronics in the Faculty of Electrical Engineering, Mathematics and Computer Science, Delft University of Technology, 2628 CD Delft, The Netherlands

CORRESPONDING AUTHOR: Y. DONG (e-mail: yicongd2@illinois.edu)

This work was supported in part by the U.S. Department of Energy through the Lawrence Livermore National Laboratory under Contract DE-AC52-07NA27344 and Contract LLNL-JRNL-830308, and in part by the LLNL-LDRD Program under Project 19-DR-015.

ABSTRACT In this work, we demonstrate and model the deep-level defect physics of semi-insulating gallium arsenide bulk photoconductive semiconductor switches (PCSS) with gap size of 10 μm and 25 μm in dark-mode operation. Experimental measurements up to biasing field of 10 kV/cm show near-bistable characteristics in the dark-mode current-voltage relations for the PCSS, which cannot be reproduced through commercial Technology Computer-Aided Design simulations. Thus, we model the PCSS by solving for homogeneous non-equilibrium steady-state of the PCSS trap dynamics, where we introduce two semi-analytical models both involving two deep levels with impact ionization effects. Both models have an excited deep-level that can capture electrons from or emit electrons to the conduction band. The two models differ, however, by the fact that one has a ground state with capture and emission, whereas the other does not include such mechanisms but instead includes electron excitation and relaxation processes directly between the ground state and the excited state without interactions with the conduction band. We find that the former does not fit with experimental near-bistable features while the latter achieves a good match with the same total number of fitting parameters. Further measurements of bias upto 50 kV/cm on one 10 μm PCSS confirms the validity of the second model as well. Finally, a brief discussion of the implications on the illuminated operation of the PCSS is also given to illustrate the importance of including defect interactions and defect avalanche effects.

INDEX TERMS Gallium arsenide, photoconductive semiconductor switch, current-voltage characteristics, avalanche multiplication, impact ionization, deep-level trap.

I. INTRODUCTION

Photoconductive semiconductor switches (PCSS) [1] are radio-frequency (RF) electronic devices with potential applications in high-frequency sampling [2], [3], large-bandwidth communications [4], [5] and high-power circuits [6], [7]. PCSS are generally fabricated from relaxation semiconductor materials [8], [9], for example, semi-insulating (SI) gallium arsenide (GaAs) [10]. These materials are selected since they are compensation-doped to increase their electric resistivity and thus their ON-OFF current ratio [11]. As a result of compensation doping, defects play a crucial role in controlling the carrier transport in SI materials [12], and there

This work is licensed under a Creative Commons Attribution 4.0 License. For more information, see https://creativecommons.org/licenses/by/4.0/

is increasing interest in obtaining useful information on the deep-level traps of SI semiconductors from the output measurements of PCSS [13].

However, many of the existing studies of trap properties in relaxation semiconductors and in PCSS are under optical illumination, [14], [15], [16]. While such studies capture the trap physics under high-level injection (HLI), measurements under the dark mode are more suitable to directly extract the trap properties and optimize the device design for its use in the illuminated mode.

In this work, we theoretically study the dark-mode current-voltage (I-V) characteristics of SI GaAs PCSS in which near-bistablility has been experimentally observed at room temperature. Bistability refers to an S-shaped Negative Differential Conductivity (SNDC) where two stable solutions of the free electron concentration are possible at the same applied electric field provided that the system has at least two deep-level defect states, so during a quasi-static measurement voltage sweep, hysteresis in current is observable [17]. When certain carrier transfer rates between the deep-level defect states overwhelm others, the semiconductor will no longer manifest true SNDC. Nevertheless, the semiconductor will display near-bistable I-V characteristics with a sudden increase in current at a critical electric field [18]. Such a near-bistable operation has been observed in the dark-mode measurements of the GaAs PCSS reported in this paper.

The experimental dark-mode I-V characteristics of GaAs PCSS discussed here cannot be reproduced via commercial Technology Computer-Aided Design (TCAD) simulations that incorporate only one trap level without avalanche effects. To resolve the discrepancy between TCAD results and experimental data, we implement two distinct custom numerical models for trap dynamics involving two trap levels, as well as trap-assisted impact ionization or avalanche. Our key finding is that only one of the two custom models in which the excited state participates in electron emission and capture processes with the conduction band can accurately replicate experimental results. Finally, we take advantage of the analysis conducted in dark mode with trap-assisted avalanche processes to draw conclusions regarding the PCSS performance in the on-state. Our dark-mode results would be useful for the illuminated PCSS because the trap kinetics influence the electrostatic screening and thus the photo-current of the device. Besides, trap-assisted avalanche processes might take place on a time-scale much faster than the low-field trapping and de-trapping of carriers. Thus, the concurrence of avalanche and optical injection processes would be crucial to understand the physics and design of the PCSS.

II. METHOD

A. EXPERIMENT

Measurements were taken on GaAs PCSS switches that followed a similar fabrication process and design that was reported in our previous work [13]. To summarize the fabrication, semi-insulating 2-inch GaAs wafer with 380 μm thickness from AXT Inc. was cleaved and cleaned in 1:1 HCl:H_2O to create 1-inch quarter. The PCSS patterns were defined with direct-write ultraviolet lithography using a Heidelberg maskless aligner and negative photoresist, three patterns total. The ohmic contacts with metal stacks of Ge (20 nm)/Au (40 nm)/Ni (10 nm)/Au (20 nm)/Ti (10 nm)/Au (200 nm) were deposited with electron beam evaporation and rapidly thermally annealed. An approximately 10 μm thick polyimide layer was spun and cured to provide dielectric protection and support for an optical aperture, made of Ti/Au, for pulse compression photoconductive switch operation, not considered in this particular study, but described in our earlier work [13]. The polyimide was then coated with a thick positive resist and etched to expose the ohmic contacts for testing.

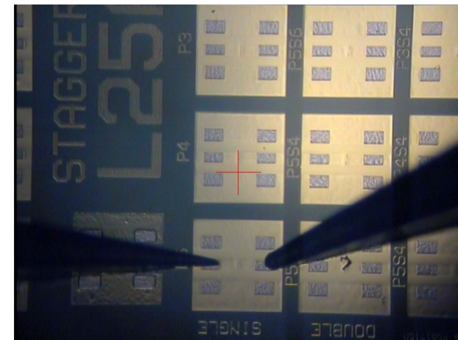

(a) Devices with 25 μm gap.

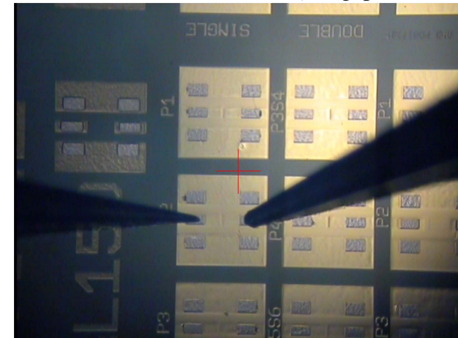

(b) Devices with 10 μm gap.

FIGURE 1. CMOS camera images of selected GaAs photoconductive switches being tested.

The devices tested in dark current mode implemented as co-planar wave-guide structures with varying gaps in the signal trace (60-μm wide) as shown in Fig. 1. The gaps tested were 10 and 25 μm. For each gap, five different devices were tested. The dark current measurements were taken in a probe station with a metal enclosure using a Keithley 4200A parameter analyzer. DC probes were placed on the open pads on both sides of the signal trace, and voltage was swept from equilibrium to 10 kV/cm equivalent average fields, in a positive direct first, and then repeated for the negative direction. An additional measurement on the 10 μm gap device was conducted up to 50 kV/cm in order to verify the high-field near bistability operation, as predicted by our models.

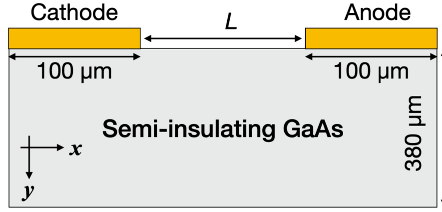

FIGURE 2. Geometric structure of the GaAs PCSS simulated using commercial TCAD.

TABLE 1. Material parameters for GaAs at 300 K.

Parameter	Symbol	Value	Reference
Bandgap	E_G	1.435 eV	[20]
Electron affinity	χ	4.1 eV	[21]
Effective conduction band density of states	N_c	4.7×10^{17} cm^{-3}	[22]
Effective valance band density of states	N_v	8×10^{18} cm^{-3}	[23]
Relative permittivity	ϵ_r	12.9	[24]

TABLE 2. Selected doping scheme of SI GaAs.

Parameter	Symbol	Value
Silicon shallow donor concentration	N_{sd}	3.8×10^{14} cm^{-3}
Silicon energy level [23]	E_{sd}	$E_C - 0.0058$ eV
Carbon shallow acceptor concentration	N_{sa}	4.1×10^{14} cm^{-3}
Carbon energy level [23]	E_{sa}	$E_V + 0.026$ eV
EL2 deep donor concentration	N_{dd}	9×10^{16} cm^{-3}
EL2 energy level [25]	E_{dd}	$E_C - 0.82$ eV

B. COMMERCIAL TCAD SIMULATION

The structure of the GaAs PCSS we simulated here is shown in Fig. 2. The separation (L) between the anode and cathode is varied, while other dimensions are fixed. First, we analyze the steady-state behavior of the device under dark-mode operation. The temperature is fixed at 300 K, and the corresponding material properties of GaAs can be found in Table 1. We consider shallow-donor-shallow-acceptor-deep-donor (SDSADD) compensation using silicon, carbon and EL2 to achieve SI properties in GaAs. This scheme allows the sample to be slightly n-doped while also maintaining resistivity close to 10^8 Ω.cm [19]. Table 2 shows the doping details.

Governing equations for the drift-diffusion simulations are the Shockley equations with spatial and time dependence not explicitly shown:

$$\nabla \cdot (\epsilon_r \epsilon_0 \nabla \phi) = -q\left(p - n + N_{sd}^+ - N_{sa}^- + N_{dd}^+\right), \quad (1a)$$

$$q\frac{\partial n}{\partial t} = \nabla \cdot \vec{J_n} - q\left(R_{SRH}^n + R_{rad}^n + R_{Auger}^n\right), \quad (1b)$$

$$q\frac{\partial p}{\partial t} = -\nabla \cdot \vec{J_p} - q\left(R_{SRH}^p + R_{rad}^p + R_{Auger}^p\right), \quad (1c)$$

$$J_n = -qn\mu_n\mathcal{E} + qD_n\nabla n, \quad (1d)$$

$$J_p = qp\mu_p\mathcal{E} - qD_p\nabla p. \quad (1e)$$

Equation (1a) is Gauss' Law, where q is the elementary charge, p is free hole concentration, n is free electron concentration, N_{sd}^+ is the ionized shallow donor concentration, N_{sa}^- is the ionized shallow acceptor concentration, N_{dd}^+ is the ionized deep donor concentration, ϵ_r is the relative permittivity, and ϵ_0 is the vacuum permittivity. We use Fermi-Dirac carrier statistics for higher accuracy in TCAD simulations, and we use Maxwell-Boltzmann carrier statistics in analytical and numerical calculations. Maxwell-Boltzmann distribution is justified in the dark-mode for a SI GaAs substrate because the Fermi level, E_F, is far from the band edges (*i.e.*, E_C for the conduction band and E_V for the valence band). At equilibrium, (1a) is equated to zero on the left-hand side to ensure charge neutrality and using Maxwell-Boltzmann statistics we obtain

$$p_0 - n_0 + N_{sd}^+ - N_{sa}^- + N_{dd}^+ = 0, \quad (2a)$$

$$p_0 = N_V \exp\left(\frac{E_V - E_F}{k_B T}\right), \quad (2b)$$

$$n_0 = N_C \exp\left(\frac{E_F - E_C}{k_B T}\right), \quad (2c)$$

$$N_{sa}^- = \frac{N_{sa}}{1 + 4\exp\left(\frac{E_{sa} - E_F}{k_B T}\right)}, \quad (2d)$$

$$N_{sd}^+ = \frac{N_{sd}}{1 + 2\exp\left(\frac{E_F - E_{sd}}{k_B T}\right)}, \quad (2e)$$

$$N_{dd}^+ = \frac{N_{dd}}{1 + \exp\left(\frac{E_F - E_{dd}}{k_B T}\right)}, \quad (2f)$$

where p_0 is the equilibrium free hole density, and n_0 is the equilibrium free electron density. The equilibrium solution of E_F and the carrier densities is obtained by iteratively solving (2a)–(2f). Our equilibrium solutions confirm that the low-field electron mobility in SI GaAs is 4588 cm^2/V.s, which is close to the wafer-specifications of 4000 cm^2/V.s. The sample resistivity, ρ, of 5.5×10^7 Ω.cm is also close to 10^8 Ω.cm as found in typical SI GaAs substrates [26], as well as close to the value reported in the wafer specification sheet.

Equations (1b) and (1c) are the electron and hole continuity equations, respectively, where $\vec{J_n}$ and $\vec{J_p}$ are the respective electron and hole current densities. R_{SRH}^n, R_{rad}^n, R_{Auger}^n are the net electron recombination rates for the Shockley-Read-Hall processes, the radiative processes, and the Auger processes. Likewise, R_{SRH}^p, R_{rad}^p, R_{Auger}^p are the corresponding terms for holes. We neglect R_{Auger} in dark-mode due to the low carrier concentrations. For simplicity, $R_{SRH}^n = R_{SRH}^p = R_{SRH}$, and $R_{rad}^n = R_{rad}^p = R_{rad}$. Then,

$$R_{SRH} = \frac{np - n_i^2}{\tau_{h0}(n + n_i) + \tau_{e0}(p + n_i)}, \quad (3)$$

$$R_{rad} = C_{rad}\left(np - n_i^2\right), \quad (4)$$

where $\tau_{h0} = \tau_{e0} = 229$ ps [27], and $C_{rad} = 2 \times 10^{-10}$ cm^{3}s^{-1} [28].

Equations (1d) and (1e) describe the electron and hole current densities, respectively, due to drift and diffusion, where $\mathcal{E}$ is the electric field, μ_n (D_n) is the electron mobility

TABLE 3. Model parameters for doping-dependent carrier mobilities [29].

Parameter	Value for electrons	Value for holes
$\mu_{\rm min}$	500 cm^2/V.s	20 cm^2/V.s
$\mu_{\rm d}$	8900 cm^2/V.s	471.5 cm^2/V.s
N_0	6.0E+16 cm^{-3}	1.48E+17 cm^{-3}
ξ	0.394	0.38

TABLE 4. Model parameters for field-dependent carrier mobilities [30].

Parameter	Value
μ_1	0
$v_{\rm sat}$	1.0E+7 cm/s
E_0	4 kV/cm
E_1	4 kV/cm
ν	0
β	4
γ	0

(diffusivity), and μ_p (D_p) is the hole mobility (diffusivity). The doping-dependent carrier mobility [29] is given as

$$\mu_{\rm low} = \mu_{\rm min} + \frac{\mu_{\rm d}}{1+\left(\frac{N_{\rm sd}+N_{\rm sa}+N_{\rm dd}}{N_0}\right)^{\xi}}, \qquad (5)$$

where $\mu_{\rm low}$ is the low-field mobility after taking doping into consideration; $\mu_{\rm min}$, $\mu_{\rm d}$, and ξ are fitting parameters whose values can be found in Table 3.

To model high-field transport, we consider a field-dependent electron mobility [30] given as

$$\mu(F_d) = \frac{\mu_{\rm low} + \mu_1 \frac{F_d}{E_0} + v_{\rm sat}\frac{F_d^{\beta-1}}{E_1^{\beta}}}{1+\gamma\left(\frac{F_d}{E_0}\right)^{\nu} + \left(\frac{F_d}{E_1}\right)^{\beta}}, \qquad (6)$$

where μ_1, $v_{\rm sat}$, E_0, E_1, ν, β and γ are fitting parameters whose values are given in Table 4, and F_d is the driving force, *i.e.*, the average electric field, $\mathcal{E}$. This is otherwise known as the Transferred Electron Effect (TEE) model [31]. It is a consequence of electron velocity overshoot when small angle forward scattering takes place with polar optical phonons. With optical deformation potential removing excess electron momentum, electrons return to steady state in the conduction band valley corresponding to a larger effective mass, which reduces their velocity at higher fields. We note that adopting the TEE model for high-field electron mobility in GaAs does not contradict the physics of the Gunn effect [32]. The formation of Gunn domains require the product, $n \times L$, to exceed 10^{12} cm^{-2} in GaAs [33] (n is the free carrier density, while L is the sample length). Since this condition is not met in the dark-mode GaAs switches analyzed here, we do not observe the N-shaped Negative Differential Conductivity (NNDC) in any of our measurements.

Trap dynamics have also been included in TCAD simulations for the deep level EL2,

$$\frac{dn}{dt} = \frac{dN_{\rm dd}^{+}}{dt} = e_{\rm dd}\big[N_{\rm dd} - N_{\rm dd}^{+}(t)\big] - c_{\rm dd}(t)N_{\rm dd}^{+}(t), \qquad (7)$$

$$e_{\rm dd} = \sigma_n v_{th}^n N_C \mathcal{F}_{1/2}\left(\frac{E_{\rm dd}-E_C}{k_B T}\right), \qquad (8)$$

$$c_{\rm dd}(t) = \sigma_n v_{th}^n n(t) = \sigma_n v_{th}^n N_C \mathcal{F}_{1/2}\left[\frac{F_n(t)-E_C}{k_B T}\right], \qquad (9)$$

where $\sigma_n = 1.8\times10^{-16}$ cm^2 is the electron capture cross section arbitrarily set close to theoretical values [34] and gives electron life time of approximately 1.5 ns, $v_{th}^n = 4.4\times10^7$ cm/s is the electron thermal velocity, $\mathcal{F}_{1/2}$ stands for Fermi integral of order 1/2, and F_n is the electron quasi-Fermi level. Because time dependence of the trap dynamics is unimportant at steady state, we will not write time dependence explicitly for analytic expressions that appear in Section II-C. The result of trap dynamics can then be substituted into (1a) to determine ϕ, as well as $\mathcal{E}$ in the PCSS at steady state.

C. SEMI-ANALYTICAL TRAP MODELING

To resolve an apparent drawback in the commercial TCAD simulations, discussed in Section III-B, we consider two semi-analytical models for trap dynamics and seek homogeneous steady-state solutions for different biases and fit to the experimental I-F_d characteristics. Unlike TCAD simulations that involve only one deep level, in both of our custom trap dynamics models, we incorporate two deep level traps. Moreover, for highly energetic electrons under large applied bias, impact ionization via deep level traps becomes important and is thus included in our model. We do not consider trap dynamics or avalanche for shallow dopants since they are almost fully ionized at room temperature if not subject to large optical injection.

The first custom model for trap dynamics is referred to as the *Doubly Model*. In this model, we consider a doubly-charged ground state (gs) $N_{\rm dd}^{2+}$, a singly-charged excited state (es) $N_{\rm dd}^{+}$, and a neutral state, $N_{\rm dd}^{0}$, of the EL2 trap in GaAs. The latter two states are capable of capturing (c) an electron from and emitting (e) an electron to the conduction band, while the ground state communicates, via electron capture and emission, with the singly-excited state. These processes are illustrated in Fig. 3 in detail. Through capture of an electron, the positively charged state of the defect decreases, whereas through emission of an electron, the positively charged state of the defect increases. In addition to the capture and emission processes, both the neutral state and the excited state can be impact ionized to provide electrons to the conduction band and subsequently transition to the next more positively charged state. For the neutral state transitioning into the excited state, we describe avalanche rate as $\alpha_{\rm es}$, while for the excited state transitioning into the ground state, we describe avalanche rate as $\alpha_{\rm gs}$.

In the second model, referred to as the *Singly Model* [18], we consider a singly-charged excited state with concentration $N_{\rm es}$ of EL2, as well as an arbitrary ground state with concentration $N_{\rm gs}$. Both these states can be positively charged or neutral depending on their electron occupancy. While the excited state participates in capture/emission processes from/to the conduction band, the ground state does not, and is thus missing $c_{\rm gs}$ and $e_{\rm gs}$ as seen in Fig. 4. The rate of electron transfer from the ground state to the excited state is

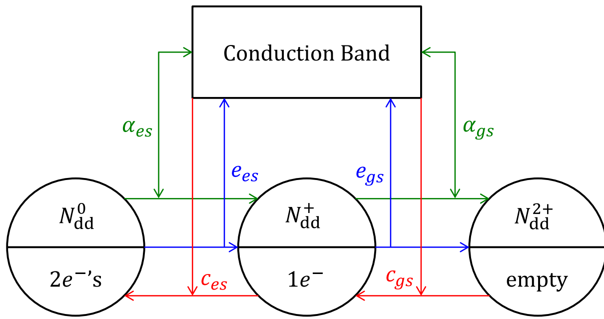

FIGURE 3. Model with doubly-charged EL2 ground state (N^{2+}_{dd}), singly-charged EL2 excited state (N^+_{dd}) and neutral EL2 state (N^0_{dd}). Arrows indicate change of states and direction of electron transfer. c_{es} is electron capture rate of the excited state, c_{gs} is electron capture rate of the ground state, e_{es} is electron emission rate of the excited state, e_{gs} is electron emission rate of the ground state, α_{es} is impact ionization rate to the excited state, and α_{gs} is impact ionization rate to the ground state.

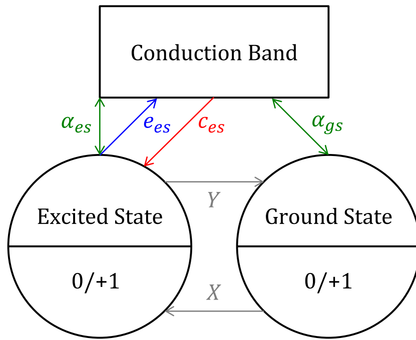

FIGURE 4. Model with two singly-charged trap states where both the ground state and the excited state can be neutral or positively charged. Arrows indicate and direction of electron transfer only. c_{es} is electron capture rate of the excited state, e_{es} is electron emission rate to the excited state, α_{es} is impact ionization rate of the excited state, α_{gs} is impact ionization rate of the ground state, *X* phenomenologically captures the excitation rate from the ground state to the excited state, while *Y* phenomenologically captures the relaxation rate from the excited state of the ground state.

denoted as X, while Y denotes the rate of electron transfer from the excited state to the ground state. Like the *Doubly Model*, the *Singly Model* also has impact ionization processes governed by avalanche coefficients of ground and excited states denoted as α_{gs} and α_{es}, respectively.

Originally, this Singly Model was proposed by Schöll for low temperature regime bistability. However, it must be noted that the previous work only studies the trap-assisted avalanche process for very low electric fields, in the range of few volts per cm, for which precise temperature conditions must be realized. On the other hand, in this work, both theoretically and experimentally, we have considered field regime up to tens of kilovolts per cm. Only when the electric fields are large enough, carriers can gain sufficient kinetic energy to cause trap assisted avalanche process. That is, the kinetic energy gained by carriers over a mean free path due to the applied electric field, ΔKE, must exceed the ionization energy of the lattice for avalanche. This is adequately expressed by the following equation:

$$\Delta\text{KE} = q\int_0^\lambda \mathcal{E}(x)\,dx, \tag{10}$$

where $\mathcal{E}(x)$ is the electric field, and λ is the mean free path. Because λ decreases at higher temperatures due to stronger carrier-phonon scatterings, the electric field must be much higher to observe the avalanche process at higher temperatures. Thus, in our samples which are measured at 300 K, we need much higher electric fields (around 3 kV/cm) than those required in Schöll's analysis of trap-assisted avalanche.

Several other works in the literature that have explored the room temperature applications of this model. For example, in [17], authors showed that the trap-assisted avalanche process at 300 K in a GaAs MESFET was the leading cause of the observed SNDC. In [35], authors used the same model to explain the switching behavior of TiN/$GeTe_6$/TiN threshold devices occurring at roughly 20 kV/cm fields at 300 K. Our most important advance with this model is its application to photoconductive switches, and we explain the details of modeling as follows.

C.1. EQUILIBRIUM SOLUTION

To begin with, we first find the equilibrium solution for the various state variables. This case corresponds to the zero bias situation where we do not observe any impact ionization of traps. In the Doubly Model, the total deep donor concentration is defined as

$$N_{\text{dd}} \equiv N^+_{\text{dd}} + N^{2+}_{\text{dd}} + N^0_{\text{dd}}. \tag{11}$$

Applying the charge balance condition and ignoring the minority holes, we obtain

$$n_0 + N^-_{\text{sa}} = N^+_{\text{sd}} + N^+_{\text{dd}} + 2N^{2+}_{\text{dd}}. \tag{12}$$

Using Maxwell-Boltzmann statistics, the ionized concentration for the various charged states of EL2 is given as

$$N^-_{\text{sa}} = \frac{N_{\text{sa}}}{1 + g_{\text{a}}\exp\left(\frac{E_{\text{sa}}-E_F}{k_BT}\right)}, \tag{13a}$$

$$N^+_{\text{sd}} = \frac{N_{\text{sd}}}{1 + g_{\text{d}}\exp\left(\frac{E_F-E_{\text{sd}}}{k_BT}\right)}, \tag{13b}$$

$$N^+_{\text{dd}} = \frac{N_{\text{dd}}}{1 + \frac{g_0}{g_1}\exp\left(\frac{E_1-E_F}{k_BT}\right) + \frac{g_2}{g_1}\exp\left(\frac{E_1-E_2+E_F}{k_BT}\right)}, \tag{13c}$$

$$N^{2+}_{\text{dd}} = \frac{N_{\text{dd}}}{1 + \frac{g_1}{g_0}\exp\left(\frac{E_F-E_1}{k_BT}\right) + \frac{g_0}{g_1}\exp\left(\frac{2E_F-E_2}{k_BT}\right)}, \tag{13d}$$

where $g_{\text{a}} = 4$ is the shallow acceptor degeneracy, $g_{\text{d}} = 2$ is the shallow donor degeneracy, $g_0 = 1$ is the N^{2+}_{dd} degeneracy, $g_1 = 2$ is the N^+_{dd} degeneracy, and $g_2 = 1$ is the N^0_{dd} degeneracy. Using E_V as the reference for energy terms, transition energy $E_1 = \epsilon_{10} - \epsilon_{00} = 0.52$ eV is difference between the N^+_{dd} states and the N^{2+}_{dd} states. Transition energy $E_2 = E_1 + E_{\text{dd}} = 0.52 + (1.424 - 0.65) = 1.29$ eV, in which

$E_{dd} = E_C - 0.65$ eV is the energy difference between the conduction band and the N_{dd}^+ states [36]. For the Doubly Model, the compensation occurs for $N_{sd} = 2 \times 10^{15}$ cm^{-3}, $N_{sa} = 2 \times 10^{16}$ cm^{-3}, $N_{dd} = 1 \times 10^{17}$ cm^{-3}, and the equilibrium $E_F = E_C - 0.62$ eV with $n_0 = 2.3 \times 10^7$ cm^{-3}.

For the Singly Model, the total deep donor concentration is defined as

$$N_{dd} \equiv N_{dd}^+ + N_{gs}^0 + N_{es}^0, \tag{14}$$

where N_{dd}^+ is the total singly-charged empty donor concentration, N_{gs}^0 is the neutral ground state concentration, and N_{es}^0 is the neutral EL2 excited state concentration. The equilibrium solution is obtained by solving the following equations:

$$n_0 + N_{sa}^- = N_{sd}^+ + N_{dd}^+, \tag{15a}$$

$$N_{dd}^+ = \frac{N_{dd}}{1 + \frac{g_1}{g_2}\exp\left(\frac{E_F - E_{es}}{k_B T}\right)}, \tag{15b}$$

$$N_{sa}^- = \frac{N_{sa}}{1 + g_a \exp\left(\frac{E_{sa} - E_F}{k_B T}\right)}, \tag{15c}$$

$$N_{sd}^+ = \frac{N_{sd}}{1 + g_d \exp\left(\frac{E_F - E_{sd}}{k_B T}\right)}. \tag{15d}$$

where $E_{es} = E_C - 0.65$ eV is the energy location of the EL2 excited state, same as in the case of the Doubly Model.

For obtaining the equilibrium solution in the Singly Model, we neglect the ground state in the charge balance equation. To avoid inaccurate final results, we only use the charge balance equations to obtain an initial guess for the equilibrium concentration, which is then used to identify the ratio X/Y that yields an optimal fit to the measured I-F_d characteristics of the PCSS. Once X/Y is extracted, the equilibrium concentrations can be automatically determined by setting $F_d = 0$. The compensation for the Singly Model is obtained for $N_{sd} = 1 \times 10^{15}$ cm^{-3}, $N_{sa} = 1.9 \times 10^{16}$ cm^{-3}, $N_{dd} = 9.3 \times 10^{16}$ cm^{-3}, $E_F = E_C - 0.61$ eV, and $n_0 = 2.48 \times 10^7$ cm^{-3}.

C.2. TRAP DYNAMICS

After obtaining the equilibrium concentrations for both the Doubly Model and the Singly Model, we solve for the trap dynamics at steady state in the presence of trap-assisted avalanche in order to match the model-generated current with the experimentally measured current in the PCSS.

For the Doubly Model, the trap dynamics equations are

$$\frac{dn}{dt} = \frac{dN_{dd}^{2+}}{dt} - \frac{dN_{dd}^0}{dt} = 2\frac{dN_{dd}^{2+}}{dt} + \frac{dN_{dd}^+}{dt}, \tag{16a}$$

$$\frac{dN_{dd}^0}{dt} = -\alpha_{es} n N_{dd}^0 - e_{es} N_{dd}^0 + c_{es} N_{dd}^+, \tag{16b}$$

$$\frac{dN_{dd}^{2+}}{dt} = \alpha_{gs} n N_{dd}^+ + e_{gs} N_{dd}^+ - c_{gs} N_{dd}^{2+}, \tag{16c}$$

$$\frac{dN_{dd}^+}{dt} = -\frac{dN_{dd}^0}{dt} - \frac{dN_{dd}^{2+}}{dt}. \tag{16d}$$

Similarly, the Singly Model has

$$\frac{dn}{dt} = \alpha_{gs} n N_{gs}^0 + e_{es} N_{es}^0 - c_{es} N_{dd}^+ + \alpha_{es} n N_{es}^0, \tag{17a}$$

$$\frac{dN_{gs}^0}{dt} = -\alpha_{gs} n N_{gs}^0 - X N_{gs}^0 + Y N_{es}^0, \tag{17b}$$

$$\frac{dN_{es}^0}{dt} = -e_{es} N_{es}^0 + c_{es} N_{dd}^+ - \alpha_{es} n N_{es}^0 + X N_{gs}^0 - Y N_{es}^0 \tag{17c}$$

In both models, we assume the van Overstraeten model [37] for avalanche rate with external bias, which gives

$$\alpha_{es} = a_{es} \exp\left(-\frac{b_{es}}{F_d}\right), \tag{18a}$$

$$\alpha_{gs} = a_{gs} \exp\left(-\frac{b_{gs}}{F_d}\right), \tag{18b}$$

where a_{es}, b_{es}, a_{gs} and b_{gs} are fitting parameters to the avalanche model. By setting all time derivatives in both (16) and (17) to zero, we obtain steady-state homogeneous solutions for the concentrations.

Knowing the steady-state concentration, n, the current versus field in the PCSS can be obtained using

$$I = qn\mu_n F_d A_{eff}, \tag{19}$$

where μ_n is again modeled using the doping- and field-dependent mobility models described in (5) and (6), respectively, and A_{eff} is the effective area of the PCSS contacts, which is related to their transfer length [38] and is estimated from the measurements.

In the Doubly Model, the electron capture cross sections σ_{es} and σ_{gs} are extracted from calibrating the model against measurements, where the standard definition for electron capture cross section (σ_n) from any deep donor state has already been given in (8) and (9). In contrast, we fix $\sigma_{es} = \sigma_{gs} = 1.81 \times 10^{-16}$ cm^2 for the Singly Model. To summarize, the seven fitting parameters for the Doubly Model are σ_{es}, σ_{gs}, a_{es}, b_{es}, a_{gs}, b_{gs}, and A_{eff}. The seven fitting parameters for the Singly Model include a_{es}, b_{es}, a_{gs}, b_{gs}, $\frac{X}{Y}$, Y, and A_{eff}.

To understand the effect of X and Y on I versus F_d in the Singly Model, we vary X/Y, while keeping all other parameters fixed. To do this, Y is fixed to an arbitrary value close to 1×10^{-11} s^{-1} while X is varied. A change in X/Y implies changing the relative rate of relaxation and excitation processes between the ground state and the excited state. When $X/Y < 1$, relaxation dominates over excitation and more defects are in their ground state, while excitation dominates relaxation for $X/Y > 1$. As shown in Fig. 5, an increase in X/Y leads to a larger deviation of I versus F_d from ohmic response. This is because the probability of carriers to be excited and thus impact ionized increases with an increase in X/Y. On the other hand, if X and Y were simultaneously increased, while keeping X/Y constant, the rate of excitation of carriers from the ground state to the excited state would increase. In this case, the knee in I versus F_d would occur at a lower field for a larger X and Y as shown in Fig. 6.

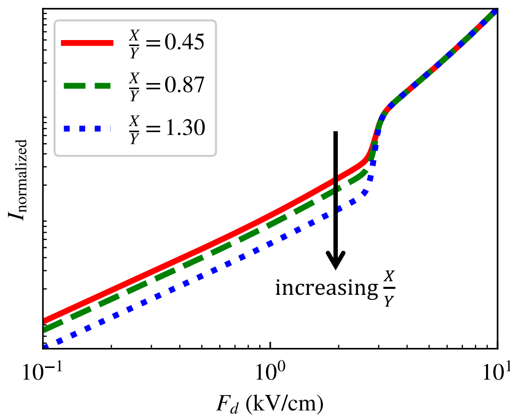

FIGURE 5. Influence of parameter $\frac{X}{Y}$ in log-log scale of normalized I vs. F_d. Here, X/Y is varied by changing X, while Y is fixed to an arbitrary value close to 1×10^{-11} s^{-1}.

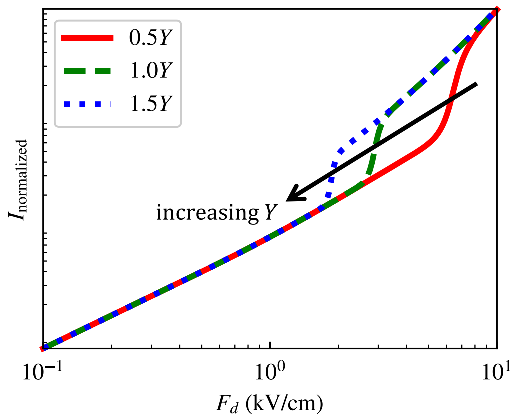

FIGURE 6. Influence of parameter Y in log-log scale of normalized I vs. F_d. Here, X/Y is fixed at 0.87, while Y is perturbed by ±50% from an arbitrary value close to 1×10^{-11} s^{-1}. As a result, X also varies by ±50%.

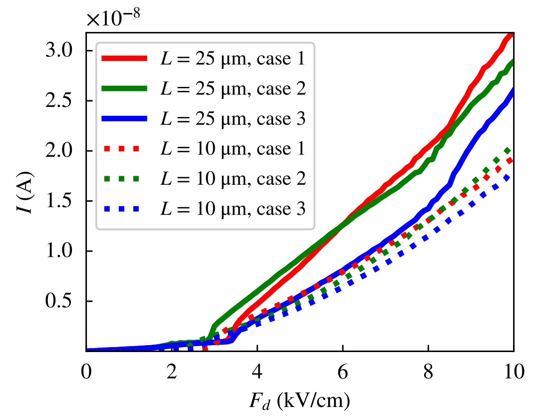

(a) Linear scale.

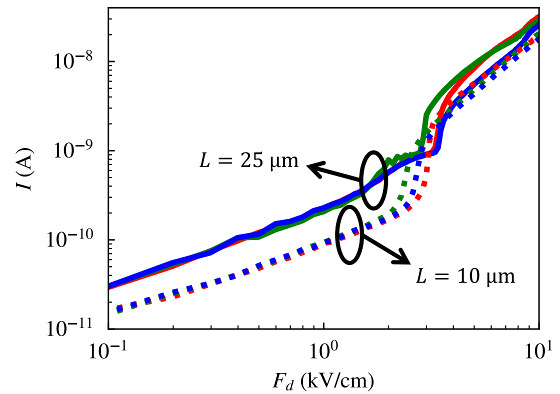

(b) Log-log scale.

FIGURE 7. Measured I-V characteristics normalized to current (I) vs. applied field (F_d) in (a) linear scale and (b) logarithmic scale. Solid traces are for $L = 25$ μm while dotted traces are for $L = 10$ μm. For each L, different color traces correspond to the different cases, as explained in the text.

III. RESULTS

A. EXPERIMENT

The three most reliable measurements out of the respective five devices of 25 μm and 10 μm gap are shown in Fig. 7. The random error in these measurements is lower as they are obtained on devices fabricated on the same wafer. Hereafter, we refer to these measurements as **case 1**, **case 2**, and **case 3** for both 25 μm and 10 μm devices. The current is presented with respect to the average applied electric field, which can be calculated from the applied voltage divided by the device gap. At approximately 3-3.5 kV/cm electric field, the current increases sharply by about an order of magnitude. This unusual non-ohmic response of the dark-mode current motivated further investigation of the underlying physics via TCAD simulation.

B. COMMERCIAL TCAD SIMULATION

We compare and contrast our TCAD results with case 1 of $L = 25$ μm and $L = 10$ μm. The TCAD framework SDSADD compensation scheme is discussed in Section II-B.

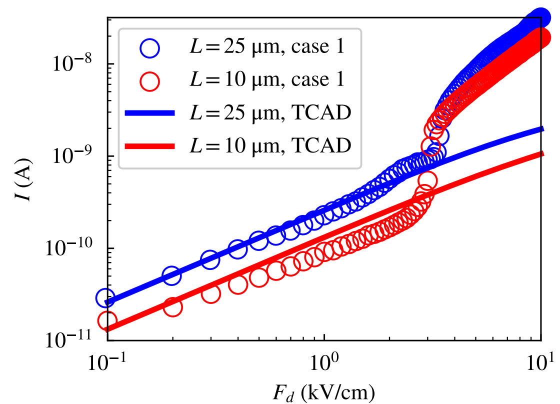

FIGURE 8. Matching case 1 of $L = 25$ μm and $L = 10$ μm with corresponding TCAD simulations.

As evident in Fig. 8, the commercial TCAD can fit to the low-field portion of the I-F_d curves relatively well. In this region, the device shows an ohmic response and by appropriately choosing electron mobility and concentration, the error between the TCAD results and experimental data can be

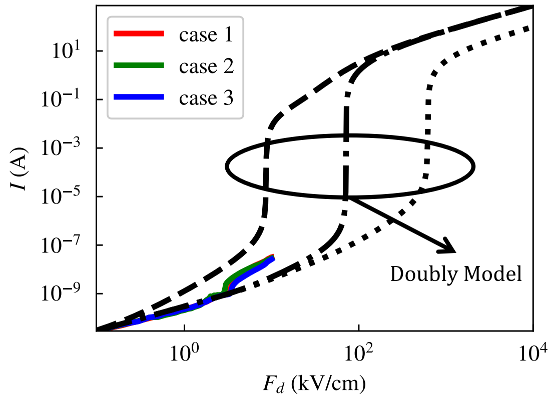

FIGURE 9. Attempts to fit $L = 25$ μm cases with the Doubly Model. a_{es} and b_{es} were tweaked in an attempt to fit to the first abrupt increase, but the model fails to capture the essential features of the measured data.

reduced. However, the TCAD models are unable to capture the increase in I at $F_d \approx 3$ kV/cm. The experimental observations cannot be explained by invoking the bulk avalanche process as it takes place at a significantly higher electric field in GaAs [39]. For similar reasons, we can also rule out Poole-Frenkel effects in our sample [40], [41]. Another common theory with regard to the SNDC is current filamentation in GaAs PCSS [42]. However, current filamentation is oftentimes observed in situations where optical carrier injection is present [43], [44], and the carrier density needs to be as high as 10^{17} cm^{-3} for filamentation at relatively low electric fields [45]. In the dark mode, the carrier concentration of GaAs is quite low as the sample is highly resistive and nearly compensated such that the essential condition to observe current filamentation cannot be satisfied in our samples. Alternatively, it has also been shown in [46] that the electric field for filamentation in GaAs can be greater than 250 kV/cm, which is also an order of magnitude higher than the electric fields considered in our work. Instead, we focus on impact ionization of traps, commonly present in SI GaAs, as the leading cause of the observed sharp increase in I at a certain electric field. Moreover, we need to invoke two traps in our models as the experimental I-F_d curves show two turning points with respect to the electric field.

C. SEMI-ANALYTICAL TRAP MODELING

C.1. DOUBLY MODEL

We apply the Doubly Model to analyze the 25 μm device for which results are shown in Fig. 9. The parameters in the Doubly Model that can be tweaked to match the measured data include σ_{es}, σ_{gs}, A_{eff}, a_{es}, b_{es}, a_{gs}, and b_{gs}. The parameters σ_{es}, σ_{gs}, and A_{eff} are field-independent and thus enable scaling the magnitude of I for a given F_d. On the other hand, parameters a_{es}, b_{es}, a_{gs}, and b_{gs} tune the I-F_d curve in two ways. These parameters shift the location of the first abrupt increase in I due to the avalanche of the excited state and can also adjust the slope of the I-F_d curve following the first abrupt increase.

Although in the Doubly Model, we could effectively control the appearance of the second knee in I-F_d curves by adjusting the avalanche parameters, this model does not allow us to control the magnitude of the current at the lower F_d (i.e., the first knee in the measurement). The reason for the lack of tunability in the Doubly Model is because any process between the three deep donor EL2 states in Fig. 3 requires some interaction with the conduction band and thus influencing n and I. This means that in the Doubly Model, the increase in output current due to the transition from low-field region to the region after avalanche of the excited state is dependent on the electric field magnitude at which the first knee of I-F_d occurs. Once we have a set field at which the first knee arises, the balance between c and e combined with α is already fixed, so the avalanche electron density and avalanche current that is in addition to the ohmic current are also fixed quantities. Thus, the independent tunability of the low field and high field characteristics is lacking in the Doubly Model. In other words, the adjustment of the onset electric field of the excited state will necessarily modify the electron concentration due to the interaction of the EL2 states with conduction band. Based on this analysis, we conclude that the Doubly Model cannot capture the essential features of the fabricated PCSS. The Doubly Model allows for observation of near-bistability but does not fit to experimental with quantitative accuracy. As a result, for the remainder of this paper, we will focus on the Singly Model in which the physics of carrier excitation and relaxation between the ground and excited states, captured via the X and Y parameters, provides a useful knob to control the current over a broad F_d range.

C.2. SINGLY MODEL

The Singly Model was first applied to analyze the I-F_d profile of the $L = 10$ μm device. For case 1 corresponding to $L = 10$ μm, we experimentally measure the dark-mode PCSS response at higher electric fields by conducting quasi-static measurements up to 50 kV/cm. However, due to the limitations of our measurement setup, for the remainder cases, we have acquired data only for fields up to 10 kV/cm. To explain experimental measurements, we use the Singly Model where all seven model parameters are adjusted to capture the increase in the measured current at around 3 and 30 kV/cm in Fig. 10. Although in our experimental setup, the electric field is restricted to $\leq$ 50 kV/cm, our model can be applied to predict the PCSS response at even higher fields, where saturation in the current is expected to emerge as shown in Fig. 10(c).

To obtain the optimal model parameters, the least-square fitting process was adopted, where the error is defined as

$$\text{square error} = \left[\log_{10}(I_{\text{fit}}) - \log_{10}(I_{\text{exp}})\right]^2. \tag{20}$$

Here, I_{fit} denotes the model-generated data, while I_{exp} refers to the data from experiments. The reason we define error in log-scale is due to the fact that the output current has values over several orders of magnitude. Once the optimal

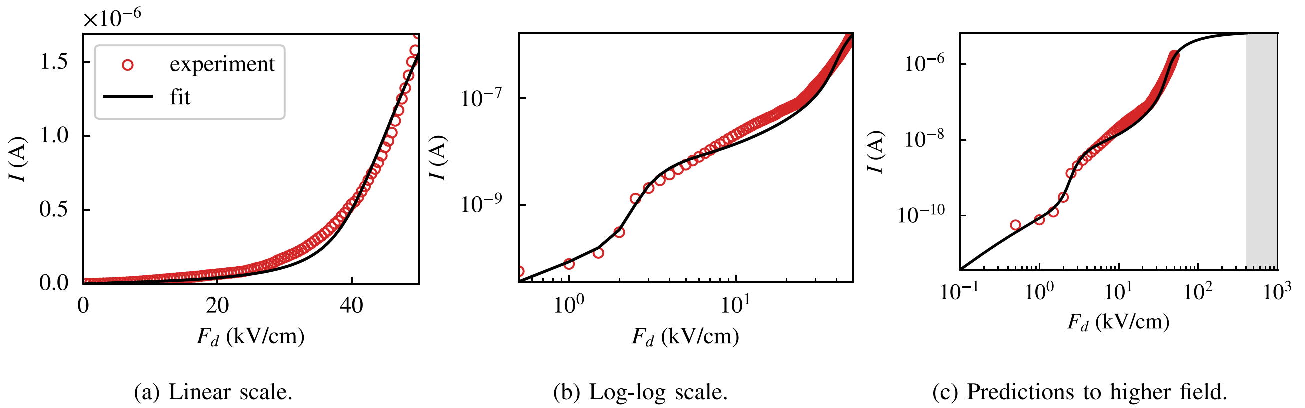

(a) Linear scale. (b) Log-log scale. (c) Predictions to higher field.

FIGURE 10. $L = 10$ μm measurement at larger $F_d = 50$ kV/cm. Grey region is bulk breakdown for GaAs. All subfigures share the same linestyles.

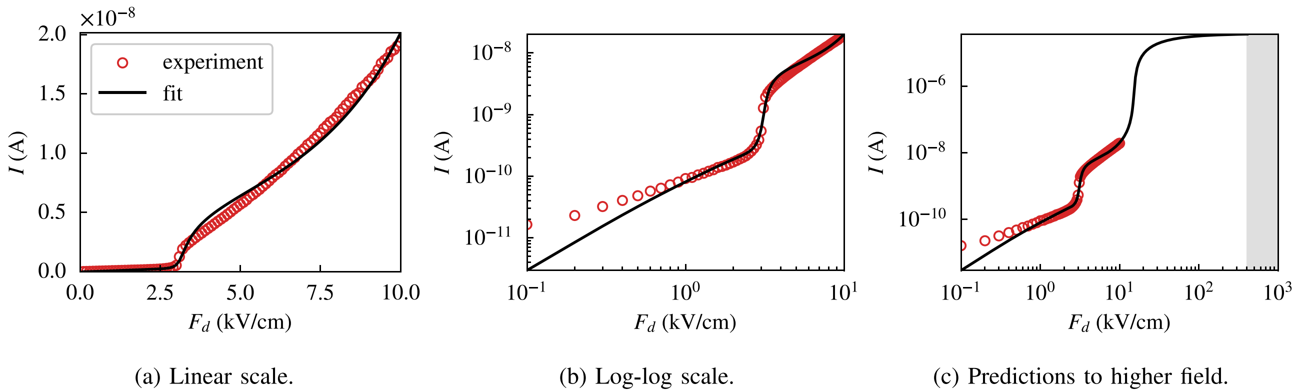

(a) Linear scale. (b) Log-log scale. (c) Predictions to higher field.

FIGURE 11. $L = 10$ μm case 1 at $F_d = 10$ kV/cm. Grey region is bulk breakdown for GaAs. All subfigures share the same linestyles.

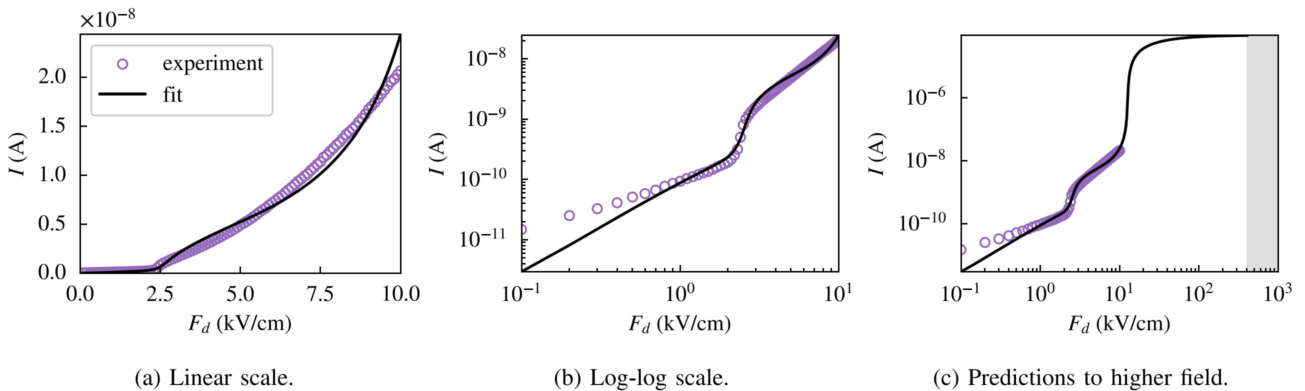

(a) Linear scale. (b) Log-log scale. (c) Predictions to higher field.

FIGURE 12. $L = 10$ μm case 2 at $F_d = 10$ kV/cm. Grey region is bulk breakdown for GaAs. All subfigures share the same linestyles.

parameters in the Singly Model are identified, the model is able to capture the measured I-F_d data accurately, both in the linear scale (Fig. 10(a)) and the log-scale (Fig. 10(b)). In this model, an optimal X/Y can be identified that allows for a precise control of the magnitude of increase in I around the first knee. We note that X/Y is manually tweaked for the minimum root mean square error (RMSE) and then kept constant throughout. The X/Y parameter is the key to accurately capture experimental near-bistability because X and Y are direct interactions between the two defect states without involving the conduction band. As a result, the magnitude of the first abrupt increase no longer depends on the knee field location. The magnitude now depends on how fast the ground state can supply electrons to the excited state as opposed to extracting them. The ratio between X and Y thus plays the role to set the magnitude of observed avalanche current that is in addition to the ohmic current. Once the ratio is fixed, we then independently tune the location of the knee through the onset avalanche field parameter of the excited state, which allows us to fit to measurements with high accuracy.

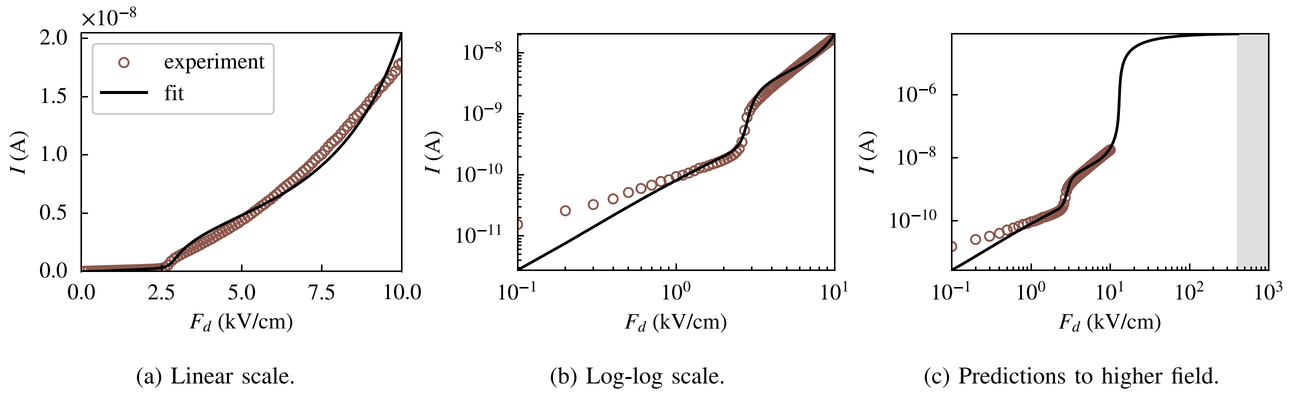

FIGURE 13. $L = 10$ μm case 3 at $F_d = 10$ kV/cm. Grey region is bulk breakdown for GaAs. All subfigures share the same linestyles.

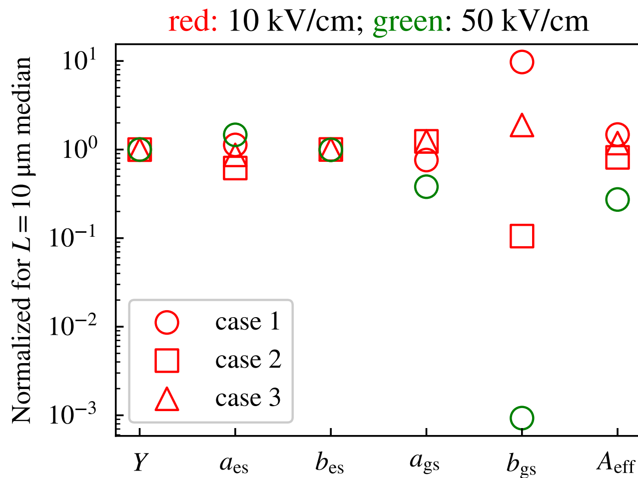

FIGURE 14. Distribution of all seven fitting parameters normalized by median that shows the robustness of fitting for $L = 10$ μm cases. Shapes represent different samples ("case") of the same length device, while color represents different bias.

Values of the fitted parameters can be found in Table 5. Our calibrated model clearly shows five distinct operation regimes in Fig. 10: the ohmic region ($F_d < 2$ kV/cm), the first abrupt increase ($F_d \approx 3$ kV/cm), the transition region [$F_d \in (3, 20)$ kV/cm], the second abrupt increase ($F_d \approx 40$ kV/cm), and the saturation region ($F_d > 50$ kV/cm).

Using $X/Y = 4.95$ as determined from the measurement of 50 kV/cm case, we calibrate the Singly Model for $L = 10$ μm up to 10 kV/cm fields as shown in Fig. 11-13. The value of X/Y greater than unity can be appreciated because the ground state needs to supply more carriers to the excited state rather than extracting them in order to assist the avalanche process of the excited state. Only when the field is large enough will the ground state also get impact ionized and produce the second abrupt increase not seen in the 10 kV/cm measurements. Fitting to the very high field and very low field regions are obviously worse in the 10 kV/cm cases, but our model can accurately capture the first abrupt increase and the transition region observed in measurements. Lack of sufficient measurement data in the low-field (high-field) regime for 50 kV/cm (10 kV/cm) fields somewhat reduces the fidelity of the model predictions. Yet, the main feature related to the trap-assisted avalanche is readily reproduced in the model for all analyzed devices.

Table 5 and Fig. 14 show that the extracted values of a_{gs} and b_{gs} parameters have a wider variation across different measurements, unlike other parameters that are more tightly controlled. As mentioned previously, this is related to the lack of measurement data at high fields. We also note that A_{eff} acts as a multiplicative factor for the current and must be smaller than the physical area of the contacts, which is respected in our parameter extraction. We have observed in TCAD simulations of illuminated PCSS that transfer length of electrons is at most one tenth of the physical length of the electrodes. For dark-mode, the conductivity is smaller, so the transfer length decreases–this is consistent with our fitted A_{eff} values that are in the range of 1/100 to 1/1000 size of physical area.

The Singly Model is also applied to the $L = 25$ μm device. The model-generated results are compared with measured data in Figs. 15-17, where all seven parameters in the model are again optimized to minimize the least-square fitting error. Once more, we observe good fitting in the first knee and the transition region. Table 6 summarizes the parameter values of all three cases corresponding to $L = 25$ μm device. The extracted parameter values, reported in Fig. 18, indicates that there is a large variation in the avalanche parameters of both the ground and excited states. Compared to all our $L = 10$ μm samples, measurement data for $L = 25$ μm have larger differences around the first knee, so the extracted parameters are unavoidably also more spread out.

D. ILLUMINATED PCSS

The dark-mode characteristics of the PCSS shed light on the underlying physics of trap-assisted avalanche mechanisms that are present in GaAs substrate. To extend our understanding to a PCSS under illumination, we perform transient homogeneous simulations of the $L = 10$ μm device. Toward this, we consider parameters from the 50 kV/cm case fitted with the Singly Model, and add an optical generation rate to (17a).

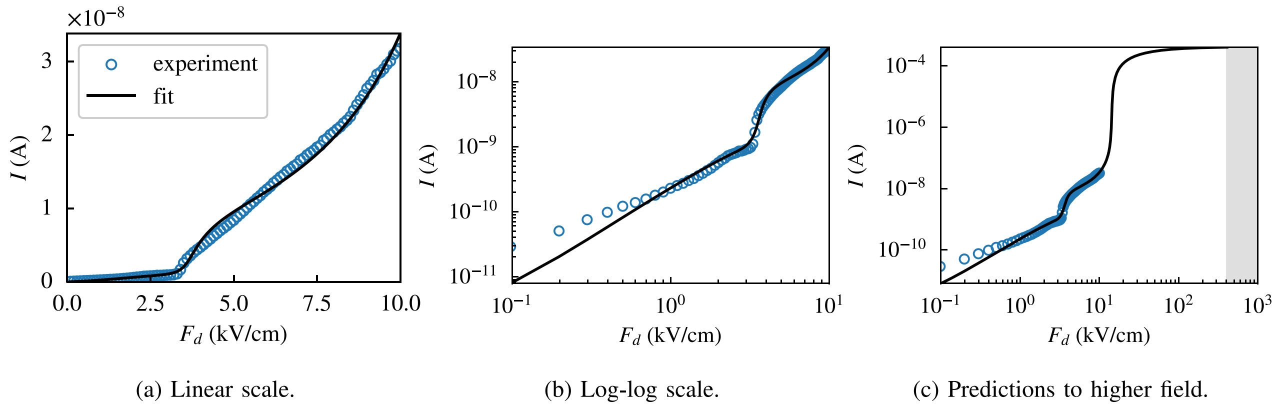

(a) Linear scale. (b) Log-log scale. (c) Predictions to higher field.

FIGURE 15. $L = 25$ μm case 1 at $F_d = 10$ kV/cm. Grey region is bulk breakdown for GaAs. All subfigures share the same linestyles.

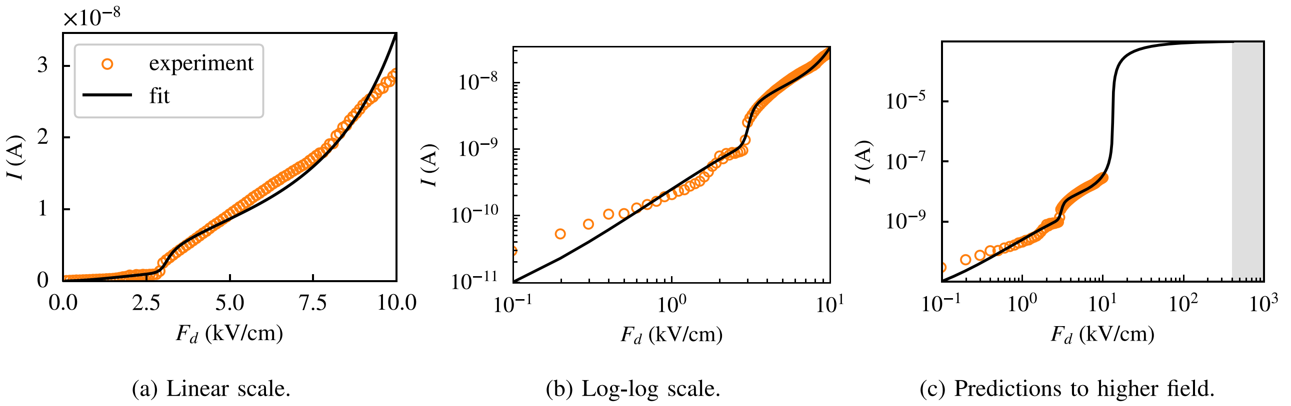

(a) Linear scale. (b) Log-log scale. (c) Predictions to higher field.

FIGURE 16. $L = 25$ μm case 2 at $F_d = 10$ kV/cm. Grey region is bulk breakdown for GaAs. All subfigures share the same linestyles.

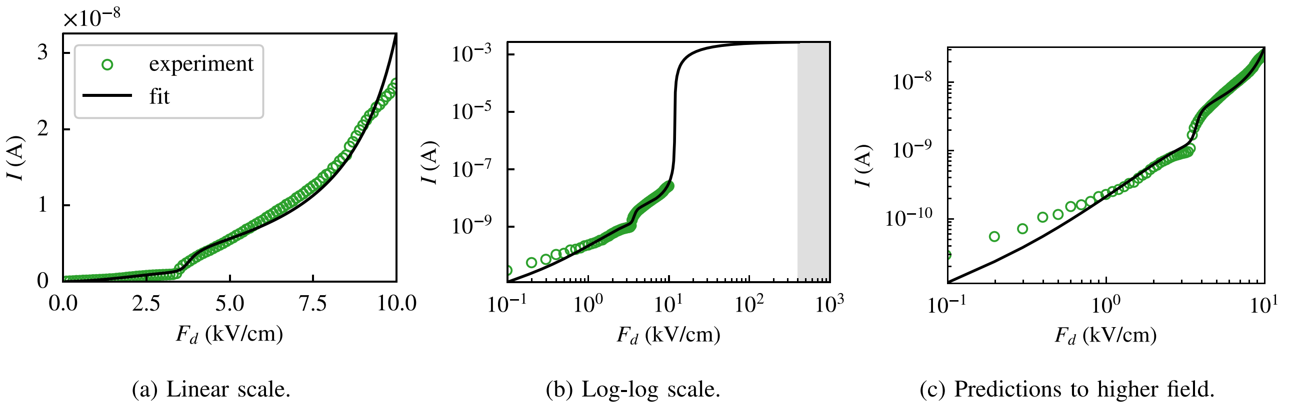

(a) Linear scale. (b) Log-log scale. (c) Predictions to higher field.

FIGURE 17. $L = 25$ μm case 3 at $F_d = 10$ kV/cm. Grey region is bulk breakdown for GaAs. All subfigures share the same linestyles.

TABLE 5. Optimization parameters for $L = 10$ μm.

Case	X/Y	Y (s^{-1})	a_{es} (cm^3/s)	b_{es} (kV/cm)	a_{gs} (cm^3/s)	b_{gs} (kV/cm)	A_{eff} (cm^2)	RMSE (A)
1, 50 kV/cm	4.95	2.56E-11	8.86E-10	0.04	1.04E-17	7.17	5.29E-07	4.92E-08
1, 10 kV/cm	4.95	1.97E-11	8.89E-10	0.08	1.09E-13	38.80	5.69E-07	5.10E-10
2, 10 kV/cm	4.95	1.08E-11	8.94E-10	0.13	1.18E-15	21.42	7.19E-07	8.66E-10
3, 10 kV/cm	4.95	1.52E-11	8.94E-10	0.13	2.12E-14	31.07	6.68E-07	6.78E-10

For simplicity, we use a square-wave pulse with optical generation rate G_{opt} and time duration Δt. We solve the system from time $t = 0$ to some $t \gg \Delta t$ when the concentration of electrons have reached a new steady-state after the optical pulse. We restrict our analysis by limiting the product $G_{opt}\Delta t$ to ensure that the shallow

TABLE 6. Optimization parameters for $L = 25$ µm.

Case	X/Y	Y (s^{-1})	a_{es} (cm^3/s)	b_{es} (kV/cm)	a_{gs} (cm^3/s)	b_{gs} (kV/cm)	A_{eff} (cm^2)	RMSE (A)
1	4.95	5.33E-09	8.98E-10	0.20	6.38E-12	39.16	2.25E-06	6.79E-10
2	4.95	8.96E-12	9.08E-10	0.34	4.95E-11	57.98	3.06E-06	1.28E-09
3	4.95	2.32E-12	9.37E-10	0.68	9.16E-11	77.48	3.64E-06	1.21E-09

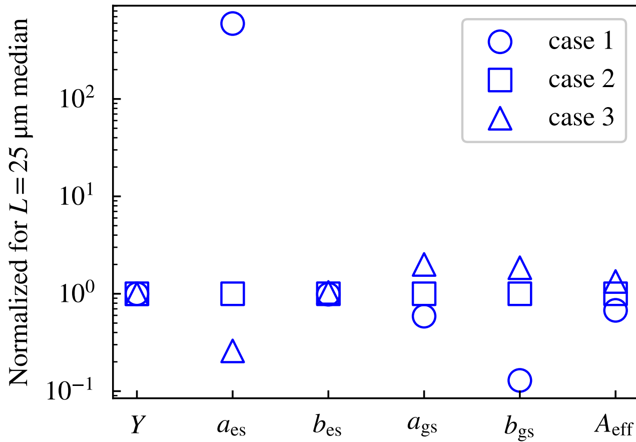

FIGURE 18. Distribution of all seven fitting parameters normalized by median that shows the robustness of fitting for $L = 25$ µm cases. Shapes represent different samples ("case") of the same length device.

dopants are still close to being fully ionized, *i.e.*, E_F is still far from the band edges, and our assumption of Maxwell-Boltzmann statistics is still valid. As illustrated in Fig. 19, we have considered three cases with combinations of $G_{opt} = 10^{25}$ $cm^{-3}s^{-1}$ & $\Delta t = 1$ ps, $G_{opt} = 10^{25}$ $cm^{-3}s^{-1}$ & $\Delta t = 10$ ps, and $G_{opt} = 10^{26}$ $cm^{-3}s^{-1}$ & $\Delta t = 1$ ps.

We find that at fixed G_{opt} & Δt combination, increasing the voltage will escalate the avalanche processes in the PCSS, which leads to a monotonic increase of the peak carrier concentration, n, as well as the full-width at half-maximum (FWHM) of the n waveform. We also find that the n waveforms of Fig. 19(b) and Fig. 19(c) look almost identical. This is because is that we are solving for homogeneous solution of the illuminated PCSS, and effects of channel length, contact length, dielectric relaxation, and recombination have been neglected. Therefore, turn-off is a much slower process than turn-on, and it is almost entirely dominated by avalanche when capture and emission in the defect level are field-independent. We also observe that N^0_{es} and N^0_{gs} do not change with time because the optical injection is not strong enough to excite a significant fraction of electrons in the occupied/unionized excited states. Thus, N^0_{es} and N^0_{gs} are only bias-dependent, but time-independent.

Figures 20 shows a comparison of the temporal profile of n for $\Delta t = 1$ ps, while Fig. 21 presents a comparison of the FWHM versus F_d for different optical injection characteristics.

We show that for a stronger injection condition, *i.e.*, $G_{opt}\Delta t$, more free electrons are available in the system, so the influence from impact ionization of deep levels will be more detrimental to the PCSS turn-off performance, especially in the negative differential mobility (NDM) regime for which $F_d > 4$ kV/cm. In fact, the devices with $F_d \geq 8$ kV/cm cannot be turned off unless we remove the electrical bias in addition to removing the optical bias. As a result, when designing a GaAs PCSS with active trap-assisted avalanche processes, low-field operation would be preferred. However, if the device is a pulse compression photoconductive switch [13], [47] that must be operated at high fields that access the NDM regime, the total laser power must be kept below a certain maximum threshold to achieve faster turn-off characteristics.

IV. CONCLUSION

In this paper, we demonstrated dark-mode I-F_d characteristics of six SI-GaAs PCSS devices, three of which have dimension $L = 25$ µm while the other three have $L = 10$ µm Experiments show a sudden increase in I when F_d is close to 3-3.5 kV/cm, which could not be captured adequately within commercial TCAD solvers. The characteristic feature in the measured current could not be explained via bulk avalanche or Poole-Frenkel emission processes as those require a much higher field in GaAs. We also exclude the possibility of filamentation since the devices examined here are not operating in the high gain mode that is featured in illuminated GaAs PCSS samples.

To explain experimental measurements, we implemented two semi-analytical models for trap dynamic–*Doubly Model* with a doubly-charged ground state, a singly-charged excited state, and a neutral state, and *Singly Model* where both ground state and excited state could be either neutral or singly-charged. In the Doubly Model, capture, emission and avalanche processes of electrons, involving the conduction band, are included. In the Singly Model, the ground state only has the avalanche process, whereas the excited state could have capture, emission and avalanche. The Singly model also includes a direct electron relaxation from the excited state to the ground state and direct electron excitation from the ground state to the excited state. We showed that only the Singly Model could faithfully reproduce the measured I-F_d profile for different length devices. This confirmed that the device exhibits at least two deep-level traps with direct electron transfer between the ground state and the excited state of the trap, without involving the conduction band. The Singly Model was used to simulate the time-domain response of the PCSS under homogeneous optical excitation. The illuminated PCSS exhibited a super-linear FWHM versus applied bias due to the avalanche process, and some of the devices with severe trap-assisted avalanche

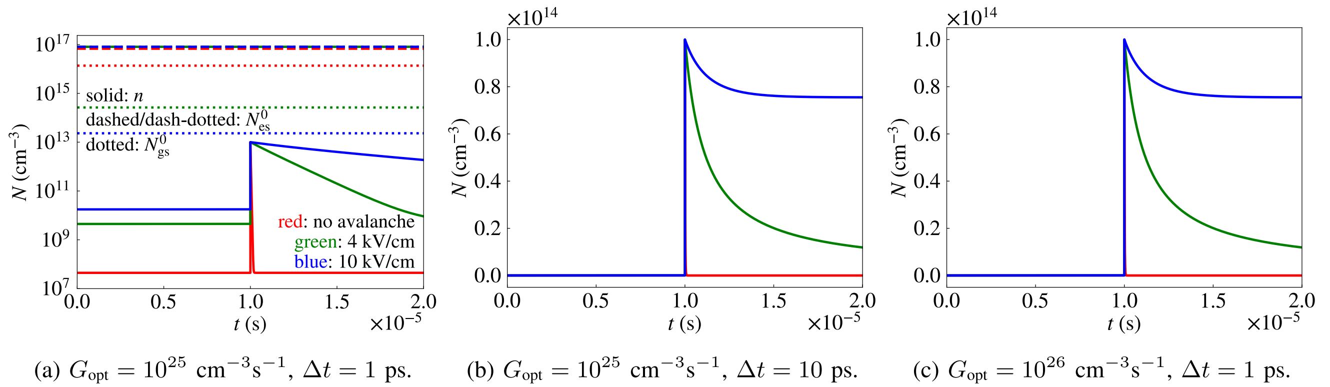

(a) $G_{\text{opt}} = 10^{25}$ cm^{-3}s^{-1}, $\Delta t = 1$ ps. (b) $G_{\text{opt}} = 10^{25}$ cm^{-3}s^{-1}, $\Delta t = 10$ ps. (c) $G_{\text{opt}} = 10^{26}$ cm^{-3}s^{-1}, $\Delta t = 1$ ps.

FIGURE 19. Density (N) evolution with time (t) for different G_{opt}, F_d, and Δt choices using parameters from the 50 kV/cm case fitted with the Singly Model. All subfigures share the same linestyles.

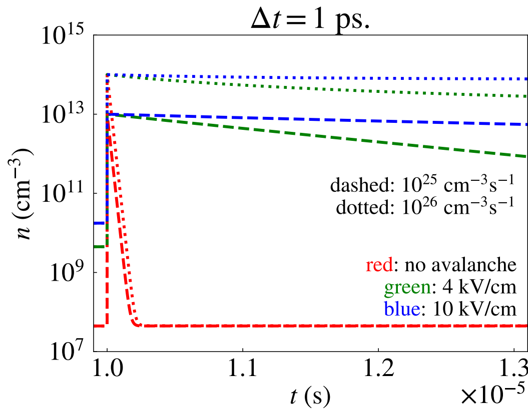

FIGURE 20. Comparing electron density evolution with time for different G_{opt}'s and F_d's at $\Delta t = 1$ ps.

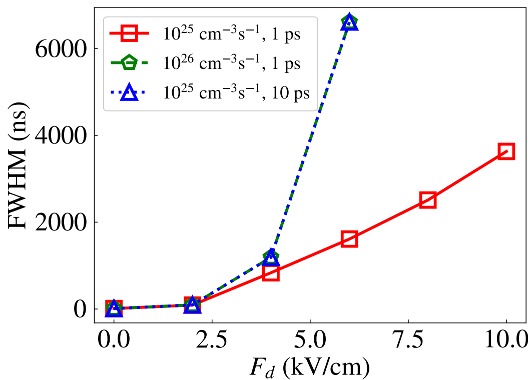

FIGURE 21. Comparing full-width at half-maximum (FWHM) of electron density evolution with F_d for different G_{opt} and Δt choices. Devices that do not turn off are not shown.

effects do not turn off. To identify the actual energy levels of defects as well as information on more minor defects, the model presented here will be complemented with Arrhenius measurements, which is part of our prospective work.

REFERENCES

[1] D. H. Auston, "Picosecond optoelectronic switching and gating in silicon," *Appl. Phys. Lett.*, vol. 26, no. 3, pp. 101–103, 1975. [Online]. Available: https://doi.org/10.1063/1.88079

[2] J. Valdmanis, G. Mourou, and C. Gabel, "Subpicosecond electrical sampling," *IEEE J. Quantum Electron.*, vol. 19, no. 4, pp. 664–667, Apr. 1983.

[3] O. Mitrofanov, I. Brener, T. S. Luk, and J. L. Reno, "Photoconductive terahertz near-field detector with a hybrid nanoantenna array cavity," *ACS Photon.*, vol. 2, no. 12, pp. 1763–1768, 2015. [Online]. Available: https://doi.org/10.1021/acsphotonics.5b00475

[4] O. Zucker and I. A. McIntyre, "Ultra wideband signal synthesis using photoconductive switches," *Microw. J.*, vol. 35, no. 7, pp. 60–68, 1992.

[5] X. Jiang, L. Guo, B. Wang, and Q. Lin, "Performance analysis for UWB system based on parallel combinatory spread spectrum using different pseudo-noise sequences," in *Proc. 2nd Int. Conf. Educ. Technol. Comput.*, vol. 4, 2010, pp. V4–213–V4–216.

[6] S. Doğan et al., "4H–SiC photoconductive switching devices for use in high-power applications," *Appl. Phys. Lett.*, vol. 82, no. 18, pp. 3107–3109, 2003. [Online]. Available: https://doi.org/10.1063/1.1571667

[7] T. S. Wolfe et al., "Integrated computational investigation of photoconductive semiconductor switches in pulsed power radio frequency applications," *IEEE Trans. Plasma Sci.*, vol. 44, no. 1, pp. 60–70, Jan. 2016.

[8] N. Haegel, "Relaxation semiconductors: In theory and in practice," *Appl. Phys. A Solids Surf.*, vol. 53, no. 1, pp. 1–7, 1991.

[9] D. D. Nolte, "Semi-insulating semiconductor heterostructures: Optoelectronic properties and applications," *J. Appl. Phys.*, vol. 85, no. 9, pp. 6259–6289, 1999. [Online]. Available: https://doi.org/10.1063/1.370284

[10] C. H. Gooch, C. Hilsum, and B. R. Holeman, "Properties of semi-insulating GaAs," *J. Appl. Phys.*, vol. 32, no. 10, pp. 2069–2073, 1961. [Online]. Available: https://doi.org/10.1063/1.1777019

[11] S. K. Mazumder, "An overview of photonic power electronic devices," *IEEE Trans. Power Electron.*, vol. 31, no. 9, pp. 6562–6574, Sep. 2016.

[12] C. Popescu and H. K. Henisch, "Minority-carrier injection into semi-insulators," *Phys. Rev. B, Condens. Matter*, vol. 14, pp. 517–525, Jul. 1976. [Online]. Available: https://link.aps.org/doi/10.1103/PhysRevB.14.517

[13] K. Dowling et al., "Pulse compression photoconductive switching using negative differential mobility," *IEEE Trans. Electron Devices*, vol. 69, no. 2, pp. 590–596, Feb. 2022.

[14] S. T. Neild, M. Skowronski, and J. Lagowski, "Signature of the gallium-oxygen-gallium defect in GaAs by deep level transient spectroscopy measurements," *Appl. Phys. Lett.*, vol. 58, no. 8, pp. 859–861, 1991. [Online]. Available: https://doi.org/10.1063/1.104513

[15] W. Shi et al., "30kV and 3kA semi-insulating GaAs photoconductive semiconductor switch," *Appl. Phys. Lett.*, vol. 92, no. 4, 2008, Art. no. 43511. [Online]. Available: https://doi.org/10.1063/1.2838743

[16] S. Mukherjee et al., "A Prony-based curve-fitting method for characterization of RF pulses from optoelectronic devices," *IEEE Signal Process. Lett.*, vol. 29, pp. 364–368, Dec. 2021.

[17] Z. M. Li, S. P. McAlister, W. G. McMullan, C. M. Hurd, and D. J. Day, "Impact ionization of deep traps in semi-insulating GaAs substrates," *J. Appl. Phys.*, vol. 67, no. 12, pp. 7368–7372, 1990. [Online]. Available: https://doi.org/10.1063/1.344523

[18] E. Schöll, "Bistability and nonequilibrium phase transitions in a semiconductor recombination model with impact ionization of donors," *Zeitschrift für Physik B Condens. Matter*, vol. 46, pp. 23–30, Mar. 1982.

[19] D. S. Mcgregor and J. E. Kammeraad, *Gallium Arsenide Radiation Detectors and Spectrometers* (Semiconductors and Semimetals), vol. 43. San Diego, CA, USA: Academic, ch. 10, pp. 383–442, 1995.

[20] Y. Varshni, "Temperature dependence of the energy gap in semiconductors," *Physica*, vol. 34, no. 1, pp. 149–154, 1967. [Online]. Available: https://www.sciencedirect.com/science/article/pii/0031891467900626

[21] S. M. Sze, *Semiconductor Devices, Physics and Technology*. New York, NY, USA: Wiley, 1985.

[22] H. Bourbaba, S. Kadri, and K. Djermane, "Optimization of the performance of GaAs solar cells: Effect of the window layer," *J. Ovonic Res. Vol*, vol. 15, no. 3, pp. 151–156, 2019.

[23] M. Brozel, *Gallium Arsenide*. Boston, MA, USA: Springer, 2007, pp. 499–536. [Online]. Available: https://doi.org/10.1007/978-0-387-29185-7_23

[24] W. J. Moore and R. T. Holm, "Infrared dielectric constant of gallium arsenide," *J. Appl. Phys.*, vol. 80, no. 12, pp. 6939–6942, 1996. [Online]. Available: https://doi.org/10.1063/1.363818

[25] Kamińska, Skowroński, and Kuszko, "Identification of the 0.82-eV electron trap, EL2 in GaAs, as an isolated antisite arsenic defect," *Phys. Rev. Lett.*, vol. 55, no. 20, pp. 2204–2207, 1985.

[26] L. Gútai, "Characterization of highly compensated semi-insulated GaAs substrates," *Acta Physica Academiae Scientiarum Hungaricae*, vol. 48, no. 2, pp. 119–130, 1980.

[27] S. Dannefaer, P. Mascher, and D. Kerr, "On the character of defects in GaAs," *J. Phys. Condens. Matter*, vol. 1, no. 20, p. 3213, 1989.

[28] U. Strauss, W. W. Rühle, and K. Köhler, "Auger recombination in intrinsic GaAs," *Appl. Phys. Lett.*, vol. 62, no. 1, pp. 55–57, 1993. [Online]. Available: https://doi.org/10.1063/1.108817

[29] M. Sotoodeh, A. H. Khalid, and A. A. Rezazadeh, "Empirical low-field mobility model for III–V compounds applicable in device simulation codes," *J. Appl. Phys.*, vol. 87, no. 6, pp. 2890–2900, 2000. [Online]. Available: https://doi.org/10.1063/1.372274

[30] K. Ashida, M. Inoue, J. Shirafuji, and Y. Inuishi, "Energy relaxation effect of hot electrons in GaAs," *J. Phys. Soc. Jpn.*, vol. 37, no. 2, pp. 408–414, 1974. [Online]. Available: https://doi.org/10.1143/JPSJ.37.408

[31] K. Hess, *Advanced Theory of Semiconductor Devices*. Hoboken, NJ, USA: Wiley, 2000.

[32] R. Van Zyl, W. Perold, and R. Botha, "The gunn-diode: Fundamentals and fabrication," in *Proc. 1998 South Afr. Symp. Commun. Signal Process.-COMSIG*, 1998, pp. 407–412.

[33] W. Kowalsky, A. Schlachetzki, and H.-H. Wehmann, "Transferred-electron domains in $In_{0.53}Ga_{0.47}As$ in dependence on the *nl* product," *Solid-State Electron.*, vol. 27, no. 2, pp. 187–189, 1984.

[34] A. Mitonneau, A. Mircea, G. Martin, and D. Pons, "Electron and hole capture cross-sections at deep centers in gallium arsenide," *Revue De Physique Appliquée*, vol. 14, no. 10, pp. 853–861, 1979.

[35] Y. Zou, D. K. Gala, and J. A. Bain, "Impact Ionization model for S-NDR based threshold switching devices," in *Proc. Device Res. Conf. (DRC)*, 2019, pp. 107–108.

[36] D. C. Look, *Defects Relevant for Compensation in Semi-Insulating GaAs* (Semiconductors and Semimetals), vol. 38. San Diego, CA, USA: Academic, 1993, pp. 91–116.

[37] R. Van Overstraeten and H. De Man, "Measurement of the ionization rates in diffused silicon p-n junctions," *Solid-State Electron.*, vol. 13, no. 5, pp. 583–608, 1970. [Online]. Available: https://www.sciencedirect.com/science/article/pii/0038110170901395

[38] M. J. Deen and F. Pascal, "Electrical characterization of semiconductor materials and devices," *J. Mater. Sci. Mater. Electron.*, vol. 17, no. 8, pp. 549–575, 2006.

[39] B. Baliga, R. Ehle, J. Shealy, and W. Garwacki, "Breakdown characteristics of gallium arsenide," *IEEE Electron Device Lett.*, vol. 2, no. 11, pp. 302–304, Nov. 1981.

[40] S. Makram-Ebeid and M. Lannoo, "Quantum model for phonon-assisted tunnel ionization of deep levels in a semiconductor," *Phys. Rev. B, Condens. Matter*, vol. 25, no. 10, p. 6406, 1982.

[41] C. Braun, T. Burke, W. T. White, and C. Dease, "The role of field enhanced emission from deep level defects in GaAs in optical switches," in *Proc. 19th IEEE Symp. Power Modulat.*, 1990, pp. 375–384.

[42] J. C. Adams, R. A. Falk, C. D. Capps, and S. G. Ferrier, "Dark current characterization of photoconductive switches," in *Proc. Opt. Activat. Switching II*, vol. 1632, 1992, pp. 110–119.

[43] G. M. Loubriel, F. J. Zutavern, M. W. O'Malley, and W. D. Helgeson, "High-gain GaAs photoconductive semiconductor switches for impulse sources," in *Proc. Opt. Activat. Switching IV*, vol. 2343, 1995, pp. 180–186.

[44] H. Liu, L. Zheng, W. Yang, X. Zhu, Y. Yang, and D. Wu, "Carrier generation in high gain GaAs photoconductive semiconductor switches," in *Proc. AOPC Adv. Laser Technol. Appl.*, vol. 9671, 2015, pp. 300–304.

[45] H. Liu and C. Ruan, "Streamer in high gain GaAs photoconductive semiconductor switches," in *Proc. IEEE Pulsed Power Conf.*, 2009, pp. 663–668.

[46] W. Shi, C. Ma, L. Hou, G. Xie, L. Tian, and S. Wu, "Velocity of current filament at the high gain mode of GaAs power photoconductive switches," *Phys. Rev. B, Condens. Matter*, vol. 406, no. 19, pp. 3741–3744, 2011.

[47] M. Xu et al., "Pulse compression characteristics of an opposed-electrode nonlinear GaAs photoconductive semiconductor switch at 2 μJ excitation," *IEEE Electron Device Lett.*, vol. 43, no. 5, pp. 753–756, May 2022.